A Theoretical Study on Superionic Behaviour of ThO_2

P. S. Ghosh*[a], A. Arya[a], N. Kuganathan[b], G.K. Dey[a], B.K. Dutta[c] and R.W. Grimes[b]

[a]Materials Science Division, Bhabha Atomic Research Centre, Mumbai-400 085, India

[b]Department of Materials, Faculty of Engineering, Imperial College, London, SW7 2AZ, UK

[c]Human Resource Development Division, Bhabha Atomic Research Centre, Mumbai 400 085, India

*Email: psghosh@barc.gov.in

Phone no.: (+91) 22-25593992 / 25595191

Abstract

This study reports density functional theory (DFT) and classical molecular dynamics (MD) calculations of lattice dynamical, mechanical and anionic transport behaviour of ThO_2 around its superionic transition temperature. Density functional theory calculated phonon frequencies were carried out under generalized gradient approximation and local density approximation with Hubbard correction as a function of isotropic dilation (ε) in lattice parameter. These indicate softening of B_{1u} and E_u mode at the X point (0, 0, 1). A nonlinear decrease of phonon modes in the $0.05 > \varepsilon > 0.04$ range is associated with a sharp increase in the narrow peak of the PDOS when the B_{1u} and E_u modes crosses each other (or about to cross) at the X point, signifying a higher occupation probability and hence a higher coupling probability of these modes at high temperatures. As a result, the probability of anions occupying interstitial sites becomes high. Moreover, our nudged elastic band MD results of diffusion barrier shows that <001> is the easy direction for anion migration. Tracking of anion positions in the superionic state as a function of time in MD simulations suggests a hopping diffusion model in which the oxygen ions move from one tetrahedral site to another via octahedral interstitial sites. These results establish the pathways within the structure that would provide an easy way for conducting anions through the structure in the neighborhood of the superionic temperature regime. Our MD calculated results of temperature variation of single crystal elastic constants show fluorite phase of ThO_2 remains elastically stable upto the superionic regime though the B_{1u} phonon mode is imaginary in that state.

1. Introduction

Many compounds, including XF_2 (X = Ca, Ba, Sr, Pb), XSi_2 (X = Mg, Sn, Ge, Pb), and XO_2 (X = Ce, Pr, Th, U, Pu), crystallize in the face-centered cubic fluorite structure (CaF_2 type), where the

cation is coordinated to eight anions, and the anion is surrounded by four cations [1]. They often show unusually high ("liquid-like") anionic conductivity (values in the range 10^{-2} -1 Ω^{-1} cm^{-1}) in the solid state far below their melting points [1]. Among them, thorium dioxide (ThO_2), a typical superionic conductor, has drawn considerable attention in recent years due to its wide applications as an ultra-high temperature material, nuclear fuel material and solid-state electrolyte [1-4]. Moreover, owing to its prominent hardness, ThO_2 has potential applications as a high-k dielectric material and a laser host [4]. Doped thoria, $(Th,M)O_{2-x}$, where M represents a dopant metal, has superior characteristics in terms of its application as a candidate solid electrolyte. This is because of considerably high O ion conductivity caused by oxygen vacancy formation on doping with lower-valent cations [1-4]. Thoria is also important for its potential use in nuclear energy applications [5-8]. Although the main fuel for present nuclear power reactors is urania-based, thoria-based fuel is attracting much attention as an alternative with potentially high performance values that can effectively lower the environmental burden mainly caused by managing and storing the long-lived highly radioactive nuclides generated in conventional spent nuclear fuel.

In the recent past, there have been a few attempts to study structural and diffusional properties of ThO_2 as a superionic conductor. Willis *et al.* [9] measured the Bragg reflections of ThO_2 by neutron diffraction in the temperature range 293-1373 K and determined mean-square thermal displacements of the atoms in ThO_2 as a function of temperature. They observed that, with the rise of temperature, the oxygen atoms tend to move from fluorite-type positions at (0.25 0.25 0.25) towards the large interstitial sites at 0.5 0.5 0.5 along <111> direction. At 1273 K, the mean atomic co-ordinates of the oxygen atoms are 0.25+δ 0.25+δ 0.25+δ, where δ = 0.014 for ThO_2. This relaxation effect indicates that either the oxygen sublattice is disordered or they vibrate anharmonically across the ideal lattice sites along the <111> directions. Similarly, Clausen *et al.* [10] and Hutchings *et al.* [11] observed the presence of Frenkel disorder of the oxygen sublattice in single crystal stoichiometric ThO_2 above 2300 K in their coherent diffuse quasi-elastic neutron scattering experiments. Their study on single crystal UO_2 also showed the presence of Frenkel disorder of the oxygen sublattice above 2000 K. The presence of Frenkel disorder was determined by allowing a fraction, n_d, of the oxygen ions to leave their regular lattice sites when fitted to the higher-temperature data. The cations were assumed to remain on their regular sites. The defective oxygen ions were assumed to occupy either or both of the two types of 'defect' sites in the 'empty' oxygen cubes: the 12 'I', interstitial sites at positions near the mid-point of the regular anion sites, such as ± (0.25+y, 0.25-y, 0), and the 8 'R', relaxed anion sites at ± (x, x, x)

relative to the cation sites. The cations were assumed to remain on their regular lattice sites and the diffuse scattering was assumed to arise primarily from anion-anion correlations. The relative population of these sites could be given by one of six different possible models as described by Dickens *et al.* [12] and designated as I-VI. The models were fitted to the data at each temperature. The measured intensities were carefully corrected for thermal diffuse scattering, extinction and absorption, before being fitted to the models. It should be emphasized that n_d includes both the true Frenkel vacancies and those arising from relaxation. It was found that the value of n_d resulting from fits to the data was relatively independent of the model used; however, the fraction of these 'vacancies' which form true Frenkel pairs was deduced from a model, and the 'best' model was taken as that one which gave the best account of both diffraction and diffuse scattering data. The simplest such cluster model was one based on a single Frenkel pair, where the interstitial is located at an 'I' site and causes its two nearest neighbours to relax towards the centre of adjacent empty cubes at 'R sites (model VI). These were labelled as 3 : 1 : 2 clusters, where the *v : i : r* notation denotes the number of vacancies : Frenkel interstitials : relaxed anions. The optimum values of x = 0.34 ± 0.01 and y = 0.05 ± 0.03 were found to be almost independent of temperature for UO_2. Similar results were also observed for ThO_2 [10,11]. Moreover, neutron scattering data showed an increase of n_d by a factor of 2.5 at temperature ~ 2800 K compared to its value at ~ 2500 K for ThO_2 [11]. Anion disorder is also reflected in the behaviour of the acoustic and optic phonon modes where neutron scattering measured lifetimes decrease rapidly. However, well defined long-wavelength acoustic modes were observed upto 2930 K, enabling the elastic constants of UO_2 to be measured upto 2930 K, indicating that their contribution to the thermal conductivity would remain significant. The inelastic scattering from lattice modes gave no indication of the nature of the electronic disorder excited in UO_2. A similar thermally induced oxygen lattice disorder was also observed in ThO_2 [11].

Indirect evidence for superionic behaviour within ThO_2 was provided by measurements of its enthalpy determined by drop calorimetry and differentiation of these data with respect to temperature to obtain specific heat (C_p(T)). Fischer *et al.* [13] measured enthalpy increments of ThO_2 using an induction heated drop calorimeter in the 300-3643 K temperature range and found discontinuities in the measured enthalpy-temperature curve. Moreover, the heat capacity value changed discontinuously from a value of 96.97 J mol^{-1} K^{-1} to 142.33 J mol^{-1} K^{-1} at 2950 K but then remained constant up to a temperature of 3643 K. They suggested that a diffuse or order-disorder phase transition occurs at approximately 80% of the melting temperature. Therefore, ThO_2 is an type II superionic material which

attains high level of ionic conductivity following a gradual and continuous disordering process within the same fluorite structure.

Moreover, Nafe *et al.* [14] analyzed the ionic conductivity of $Th_{1-x}Y_xO_{2-0.5x}$ ($0.05 \leq x \leq 0.29$) compounds over a wide temperature range (between 300-2000 K) and suggested that at low and medium temperatures, the ionic conductivity increases with temperature at a higher rate in compounds having high Y concentrations. As higher Y doping concentrations leads to the creation of higher oxygen vacancy concentrations, this implies higher anionic conductivity with increasing of temperature. But at temperatures above 1500 K, the ionic conductivity reaches a saturated value irrespective of doping concentration. Similarly, Hohnke *et al.* [15] emphasized that electrical transport occurs by thermally activated hopping of oxygen ions via empty anion sites which reaches a maximum at x~0.07 for $(Th,D)O_{2-x}$ (D=trivalent cation doping) regardless of dopant size and charge (below 1673 K). These results clearly indicate that the mechanism responsible for high ionic conductivity above 2000 K is fundamentally different from thermally activated oxygen hopping mechanism purely mediated by vacancies occurring at lower temperatures.

It is now well established that cubic fluorite structured materials undergo a transition to the "superionic" regime at temperatures close to, but below, their melting points. This transition is associated with (i) a dramatic increase in ionic conductivity [11,16-17] although electronic conductivity remains low (ii) dynamic disorder in the anion sublattice. However the details of anion transport mechanisms are still not completely understood [11,17-21]. Moreover, it is essential to understand microscopic mechanism responsible for macroscopic superionic conduction. Within the literature, the study of high temperature superionic transition in UO_2 has remained a subject of interest motivated by its use as a nuclear fuel [1,10-11,22-23]. Nevertheless, very little attention has been paid to other fluorite group members (*e.g.,* ThO_2). With renewed interest in studying the feasibility of thoria-based materials as fuel for various reactor systems, it is essential to study structural stability at extreme thermodynamic conditions. In the halide compounds, the superionic transition temperature (T_c) is typically $\sim 0.8T_m$ (T_m = melting temperature). For ThO_2, which has a T_m = 3600 K, a superionic transition might then be expected to occur at $T \sim 2900$ K. Although this is well above normal reactor operating temperatures, a detailed knowledge of the anion diffusion properties of ThO_2 is essential for fuel design, performance modeling and safety analysis [5-8]. Furthermore, the presence of an additional component in the heat capacity C_p (due to the onset of any thermally induced Frenkel

disorder) has important consequences when assessing the outcomes of possible reactor accident scenarios.

The main objectives of the present study are: (i) to study ground state lattice, lattice dynamical and mechanical stability of thoria as a function of isotropic lattice strain (dilation) using first-principles calculations and (ii) to determine the probable directions of diffusion and actual diffusion paths of the oxygen atoms in the superionic regime using classical molecular dynamic simulations. In these calculations isotropic dilation in lattice parameter (ε), defined as

$$\varepsilon = \frac{a - a_0}{a_0}$$

(a_0 = equilibrium lattice constant and a = strained lattice constant), is a manifestation of the high temperature environment in pure ThO_2. Using density function theory (DFT), the phonon dispersion curves have been calculated as a function of ε to study dynamical stability of ThO_2 as a function of temperature. Classical molecular dynamics simulations have been performed to determine the easy direction of movement, actual migration pathway of oxygen atoms, and mechanical stability of the structure which is necessary to understand the diffusion mechanism in the superionic region.

2. Computation Methodology

The Vienna ab initio simulation package (VASP) was employed in this study to perform the DFT based electronic structure calculations where the Kohn-Sham equations are solved using a plane wave expansion for the valence electron density and wave functions [24,25]. The interactions between the ions and electrons are described by the 'Projector Augmented Wave' (PAW) potentials, which use smaller radial cutoffs (core radii) and reconstruct the exact valence wave function with all nodes in the core region [26]. The PAW potentials used in this study are those provided in the VASP database which treates thorium $6s^2\ 7s^2\ 6p^6\ 6d^1\ 5f^1$ and the oxygen $2s^2\ 2p^4$ electrons as valence electrons. The exchange-correlation effects were treated using the local-density approximation (LDA) in the Ceperley-Alder parametrization and generalized gradient approximation (GGA) in the Perdew-Burke-Ernzerhof parametrization [27] within VASP. The Hubbard U correction was introduced with LDA using the method as proposed by Dudarev *et al.* [28], in which the U parameter (reflecting the strength of on-site Coulomb interaction) and J parameter (adjusting the strength of exchange interaction) are combined into a single parameter $U_{eff} = U\text{-}J$ to take care of the Coulomb repulsions between the localized f-electrons. To decide upon a suitable value of U_{eff}, available experimental data for ground state

properties (*e.g.*, lattice constant, bulk modulus and electronic band-gap) were compared with LDA+*U* calculated values. All the calculations were performed with plane wave cutoff energy of of 600 eV. The total energy of ThO_2 was optimized with respect to volume (or lattice parameter) and atomic positions. The conjugate gradient algorithm was used for the unit-cell relaxations until the residual forces and stress in the equilibrium geometry were of the order of 0.005 eV/Å and 0.01GPa, respectively. A 16x16x16 k-point meshes was constructed using the Monkhrost-Pack scheme to sample the Brillouin zone [29], which provided convergence in the total energy up to 0.0001 meV/atom.

To calculate phonon frequencies of ThO_2, the small displacement method as implemented in the PHONOPY [30] program were employed. In this methodology, the dynamical matrix is derived by giving small displacements to the atoms in the supercell from their equilibrium positions and calculating the resulting forces within the DFT framework. The phonon dispersion of ThO_2 at different lattice parameters was calculated using the GGA and LDA+*U* by giving appropriate atomic displacements in a 3x3x3 (81 atoms) supercell. For the supercell force calculations a k-point mesh of 8x8x8 was used. The splitting between the longitudinal optical (LO) and transverse optical (TO) phonon modes was corrected using a non-analytical correction term [31-33]. For the calculation of Born effective charges and high frequency dielectric constants at different values of lattice strain, a linear response method was employed as implemented in VASP. For the ab-initio part of this study, the temperature effects are considered indirectly by considering isotropic dilation of the lattice parameter.

The MD simulations to study thermal, mechanical and anion transport properties were carried out using the LAMMPS [34] code. Coulombic interactions were calculated using the Ewald method [35] with the particle–particle particle–mesh (PPPM) implementation of the method within the MD calculations to improve computational efficiency [34]. An interatomic potential of ThO_2, which combines Buckingham-Morse functional form with many-body interactions [36] was used. In the present study, the MD supercell was constructed, having 4000 cations and 8000 anions by an array of 10x10x10 unit cells of ThO_2. These structures were equilibrated with 1 fs time steps in the temperature range between 300 K and 3500 K (100 K interval) with the NPT ensemble (constant number of particles, pressure and temperature) at zero external pressure using the Berendsen barostat with a time constant of 5 ps and the Nose´-Hoover thermostat with a time constant of 1 ps. Each simulation of thermal expansion, mean-square displacements, radial distribution functions was carried out initially for 200 ps for equilibration at the desired temperature and then for another 50 ps to get an average value of the thermodynamic quantity.

To calculate the temperature dependent elastic constants, C_{11}, C_{12} and C_{44}, a stress-strain method was applied just after the system was equilibrated within the NPT ensemble at zero external pressure for 200 ps at the desired temperature. In the stress-strain method, positive and negative box displacements (deformation) were applied in all the symmetry directions and the resultant changes in stress is computed to determine elements of the elastic stiffness tensor. The deformation magnitude in the stress-strain calculations were varied from 10^{-6} to 10^{-3} in six equal steps (steps of 50 X) to ensure converged values of C_{11}, C_{12} and C_{44}. From the calculated values of C_{11}, C_{12} and C_{44} poly-crystalline Young and shear moduli were calculated using the Voight-Reuss-Hill approximations [37].

3. Results and Discussion

A. Ground state properties of ThO_2

Table 1 compares our GGA and LDA+U calculated values of equilibrium lattice constant (a_0), bulk modulus (B_0), pressure derivative of bulk modulus (B_0'), single crystal elastic constants (C_{11}, C_{12} and C_{44}), high frequency dielectric constants (ε^{∞}) and Born effective charges (Z^*) of ThO_2, with previously reported theoretical and experimental values in the literature [38-44]. **Figure SI-1 (supplementary information)** shows variation of equilibrium lattice constant (a_0), bulk modulus (B_0) and electronic energy-gap (E_g) as a function of U_{eff} calculated for LDA+U where experimental values are presented as horizontal solid lines. Analysis of this figure shows that the Hubbard-type on-site electronic interaction with value U_{eff} = 5 eV gives better prediction of experimental data (shown in **Table 1**) which is also consistent with a previous theoretical study [44]. Our LDA+U calculated a_0 is in excellent agreement (< 0.01%) with experimentally reported values at room temperature, but our GGA-PBE calculated value is overestimated (by 0.3%). Our GGA and LDA+U calculated values of B_0 underestimate (4-6%) and overestimate (5.5-7%) experimentally reported values [38,39], respectively. Our GGA and LDA+U calculated values of B_0' match well with the experimentally reported value by Idiri *et al.* [39] (high pressure synchrotron X-ray diffraction data) but underestimate (by 20%) the value reported by Olsen *et al.* [38] (high pressure XRD). Our GGA calculated elastic constants match well (< 4%) with single crystal ThO_2 elastic constant data measured by Mecedo *et al.* [40], but these values are underestimated compared to those calculated from the inelastic neutron scattering data of Clausen *et al.* [41]. Our GGA and LDA+U calculated values of ε^{∞} (4.83 and 4.74, respectively) are in good agreement with the experimental value (4.86) determined by Axe *et al.* [42]. Our GGA and LDA+U calculated Z^* for Th and O (Z^*_{Th}=5.41, Z^*_{O}=-2.71 and Z^*_{Th}=5.38, Z^*_{O}=-2.69, respectively) are in

good agreement with previous theoretical calculations [43,44]. Moreover, our theoretically calculated values of a_0, B_0, B_0', C_{11}, C_{12}, C_{44} and ε^{∞} are in good agreement with GGA and LDA+*U* calculated values by Lu *et al.* [43] and Sevik *et al.* [44], respectively. Therefore, both GGA and LDA+*U* provide comparable descriptions of ground state properties of ThO_2 and therefore both these approximations were considered for the determination of lattice dynamical properties of ThO_2 as a function of isotropic dilation in lattice parameter.

B. Lattice Dynamical Properties of ThO_2

Our GGA and LDA+U calculated phonon dispersion curves (shown in **Figure 1**) are compared with the inelastic neutron scattering measurements of Clausen *et al.* [41] at 293 K and Raman scattering measurements of Jayaraman *et al.* [45] at 295 K. These experimental measurements were performed at room temperature and more accurate comparison of calculated phonon frequencies at special symmetry k-points can be made by performing an LDA+*U* calculation of phonon dispersion with an expanded lattice taking into account the thermal expansion of ThO_2 to room temperature (9.5-10 x 10^{-6} K^{-1}) [23]. In that sense, our GGA calculated phonon frequencies should reflect thermal expansion effect. A comparison of LDA+*U* calculated phonon frequencies across the high symmetry paths with neutron scattering data shows that our LDA+*U* results agree well with experimental data in reproducing acoustic phonon frequencies. In almost all symmetry directions of phonon dispersion curve GGA calculated phonon frequencies are lower compared to LDA+*U* calculated values. In this study, the calculations for phonon dispersion curve were performed on a 3x3x3 supercell with 81 atoms. We checked convergence of LDA+*U* calculated phonon frequencies by performing a similar calculation (small displacement method) with a 4x4x4 supercell of 192 atoms and results are shown in **supplementary information (Figure SI-2)**. A comparison of the phonon dispersion curves calculated with 81 atoms and 192 atoms supercell shows frequency values calculated with smaller supercell match within 5% of frequency values calculated with the larger supercell. So, further calculations of the phonon dispersion curve as a function of isotropic dilation in lattice parameter were performed with the 3x3x3 supercell.

In **Table 2**, we enlist out GGA and LDA+*U* calculated phonon frequencies as well as experimentally measured phonon frequencies at high symmetry points of the Brillouin zone, viz., Γ, X and L. Our LDA+*U* calculated phonon frequencies of F_{1u} (LO) and F_{2g} mode matches well, within ~1% of the neutron scattering and Raman scattering data. However, the LDA+*U* calculated F_{1u} (TO) mode

overestimates experimental data by ~7% and the GGA calculated value underestimates experimental data by ~7%. At the X point, our LDA+*U* calculated phonon frequencies of E_u (acoustical mode) and E_u (optical mode) match well with inelastic neutron scattering measured frequencies but for the E_g mode, the LDA+*U* calculated value is overestimated by ~23% compared to neutron scattering data. Overall optical phonon frequencies are lower for GGA calculations compared to those of LDA+*U*. The experimentally measured E_u mode [41,45] matches well with calculated values. At the L point, our LDA+*U* calculated phonon frequencies for E_u (acoustical mode), A_{1u} and E_g matche very well with inelastic neutron scattering measured frequencies [41]. Conversely, LDA+*U* calculated E_u (optical) and A_{1g} mode frequencies are overestimated. Moreover, our GGA calculated values are always underestimated compared to experimental vales [41,45].

C. Lattice Dynamical Properties as a function of isotropic strain

Figure 2 shows our GGA and LDA+*U* calculated phonon dispersion curves and density of states (DOS) for ThO_2 at different lattice strains (dilation). It is important to note that overall as ε increases the phonon frequencies decrease as the material itself becomes softer. The singlet B_{1u} mode softens considerably as a function of ε at the X point compared to other modes. The E_u doublet mode also softens but the rate of softening of E_u is small compared to the B_{1u} mode. The singlet B_{1u} mode crosses the E_u doublet in the range $0.04 < \varepsilon < 0.045$ and $0.045 < \varepsilon < 0.05$ for GGA and LDA+*U* calculated phonon frequencies, respectively. A maxima in the phonon DOS in the low frequency region can also be observed at $\varepsilon = 0.04$ and $\varepsilon = 0.05$ for the GGA and LDA+*U* calculated DOS. A sharp increase in the phonon DOS is observed at the frequency where the B_{1u} mode intersects the E_u mode (or close to it) at the X point. The crossover of the B_{1u} and E_u modes can be clearly observed in **Figure 3,** where the variation of the B_{1u} and E_u modes is plotted a function of isotropic lattice strain.

Experimentally determined temperature variation of lattice parameters data for ThO_2 shows, 3.8% and 4% lattice strain correspond to □3500 K and □4000 K, respectively [46]. Our GGA calculated B_{1u} mode gets soften with increasing ε and becomes imaginary in the range $0.04 < \varepsilon < 0.045$. Therefore, our GGA calculated results predict a overestimated lattice parameter (or corresponding temperature) to achieve superionic state compared to those reported experimentally. This can be attributed to the following facts: (i) assumption of small displacement method (or harmonic

approximations) to calculate phonon dispersion curve is not valid upto a temperature range which is very close to melting temperature and anharmonic effects are expected to take over harmonic behaviour (ii) GGA approximation is reasonably good to predict ground state structural and mechanical properties of ThO_2 but might fail to predict those properties at elevated temperatures.

D. B_{1u} and E_u phonon mode softening at the X point

Figure 3 emphasizes an almost linear decrease of GGA and LDA+U calculated for the B_{1u} and E_u mode frequencies from $\varepsilon = 0.0$ to 0.04. After $\varepsilon > 0.04$, these mode frequencies decrease nonlinearly and the B_{1u} mode frequencies becomes smaller compared to E_u mode frequencies in the range $0.05 > \varepsilon > 0.04$. It was mentioned earlier that there is an increase in the narrow peak in the PDOS when the B_{1u} and E_u modes cross (or are about to cross) at the X point. In other words, the occupations of these modes are higher at high temperatures and possibility of the coupling of these two modes is also high.

The singlet B_{1u} mode consists of O ions motion in the [001] direction as shown in **Figure 4**. If we consider O atoms in the ThO_2 unitcell as a row of atoms along [001] direction, then atomic rows present along the [110] direction (and equivalent directions) move in phase and adjacent atomic rows move opposite in phase. On the other hand, doubly degenerate E_u mode consists of simultaneous Th and O movement's perpendicular to [001] direction. **Figure 4** also shows GGA and LDA+*U* calculated variation of the potential energy versus zone center phonon mode B_{1u} in terms of the normalized atomic displacement of O atoms as a function of isotropic dilational lattice strains. For $\varepsilon = 0$, the effective potential has a minimum at zero atomic displacement. With increasing ε (or temperature, $\varepsilon = 0.045$), the effective potential transforms into double well from a single well having maxima at equilibrium atomic position. In other words, interstitial positions become energetically favorable for oxygen atoms to occupy compared to their ideal lattice sites for $\varepsilon = 0.045$ and above. It is also important to note that, the effect of ε on the GGA calculated potential energy is more severe than the LDA+*U* calculated potential energy. This can also be understood from the calculated phonon frequencies as a function of ε curve (**Figure 3**) which shows less softening of the B_{1u} mode for LDA+*U* values compared to GGA.

E. Anion conduction mechanism

Systematic vibration of oxygen atomic rows along <001> directions leads to a singlet B_{1u} phonon mode. Similarly, a systematic vibration of Th and O atoms perpendicular to the <001>

directions (*i.e.,* in the (110) planes) leads to the E_u phonon mode. At lower values of ε (ε < 0.04), these two modes remain uncoupled and mode frequencies decrease almost linearly with ε. Moreover, the amplitude of vibration of the O atoms along <001> is higher compared to its amplitude of vibration perpendicular to <001>. With increasing ε (0.04 < ε < 0.05), the amplitude of vibration perpendicular to <001> increases and the dynamics of O atoms corresponding to B_{1u} and E_u phonon modes become coupled, which can also be manifested by a sharp increase of the narrow peak in the PDOS when the B_{1u} mode frequency become smaller than the E_u mode in the phonon dispersion curve. In other words, coupling of the B_{1u} and E_u phonon modes increases the possibility to occupy the interstitial site at temperatures close to T_c. The transformation of the potential energy landscape from single well to double well (|ε| > 0.04) emphasizes how anions preferentially migrate to interstitial sites along <001>, which essentially leads to Frankel-like positional disorder. With further increase of ε, the B_{1u} phonon mode frequencies become imaginary which leads to thermally activated complete disordering of the anion sublattice. Coupling of the B_{1u} and E_u phonon modes changes the superionic conductivity regime, where anionic conductivity is mediated by random anion hopping to interstitial sites along <001> from correlated anionic motion at interstitial sites F1 ((48 g) wyckoff positions) and F2 ((32 f) wyckoff positions).

Gavartin *et al.* [46] calculated phonon dispersion curve and PDOS of Li_2O at 10 K and 1000 K using the quasi-harmonic approximation and MD simulations and found a cross over of the transverse Raman mode (TR) and the LO mode as temperature reaches the fast-ionic phase transition point. Their explanation attributed this to a change in cationic conductivity mechanism. Mode softening leads to the loss of the relative phase of Li^+ ions moving along the [100] crystal direction (as the TR mode disappears), so that the ionic motion can be considered as a set of coupled oscillators. As soon as a few neighboring ions get in phase, a large amplitude coherent motion rapidly develops along <100>. Such fluctuations propagate a caterpillar-like mechanism, whereby a Li^+ ion moves into the cube-interstitial position, while the rest of the chain of ions moves simultaneously along <100>, each ion filling the site vacated by its nearest-neighbour. Thus, an interstitial ion and a cation vacancy, separated by a few unit cells, can be created within the same elementary act. With further increase of temperature, cations transport is mediated through a hopping mechanism. We believe an equivalent anionic conduction mechanism is followed in ThO_2.

F. Migration barrier for oxygen movement

In order to further gain insight into the anionic conduction mechanism near the superionic transition point we performed MD simulations to calculate migration barriers along different symmetry directions and to trace the actual oxygen trajectory as a function of time in the superionic state. The migration barrier for oxygen movement was calculated by creating a oxygen vacancy in a regular lattice site and moving another neighboring oxygen atom from its initial lattice site towards the vacant lattice site along [001], [110], and [111] high-symmetry directions. For this calculation a 10x10x10 supercell was employed and the charge neutrality of the supercell was maintained throughout the complete process. For this purpose nudged-elastic-band (NEB) method [47-49] was employed as embedded in LAMMPS. In this calculation 6 intermediate states were inserted and diffusion barriers were calculated. This enabled us to identify the easy direction for oxygen motion towards the vacant site in normal and superionic states. **Figure 5** shows the NEB calculated oxygen migration barrier along [001], [110] and [111] high symmetry direction for lattice parameter a = 5.6 Å (corresponding to the normal state) and a = 5.8 Å (corresponding to the superionic state). The MD NEB calculated oxygen migration barriers along [001], [110] and [111] directions are 0.78 (0.17), 4.77 (4.47) and 5.24 (5.02) eV, respectively, for lattice parameter a = 5.6 Å and a = 5.8 Å. From this analysis it is evident that the <001> directions are most favorable for oxygen atom movement in normal and superionic states.

G**. Position-Time plot for oxygen migration**

In order to identify the superionic transition temperature (T_c) for ThO_2 as predicted by the potential used in our MD simulations, we initially determined the mean square displacements (MSD), radial distribution functions (RDF) and diffusion coefficients of oxygen atoms in the temperature range 2500-3500 K (in 100 K intervals). The MD calculated values of MSD, diffusion coefficients and the RDF of oxygen atoms as a function of temperatures are plotted and results are shown in **supplementary information (Figure SI-3, 4 and 5)**. From the analysis of MD calculated MSD, RDF and diffusion coefficients of oxygen atoms shows that the superionic regime was obtained at 3000 K.

The snapshot of migration for oxygen atoms at 3000 K are shown in **Figure 6** as a position-time plot for 20 ps time duration in the XY and YZ plane. For this calculations, a 10x10x10 ThO_2 supercell was initially equilibriated as an NPT ensemble at 3000 K for 50 ps and at this temperature and the MD calculated equilibrium lattice parameter is 5.803 Å. Then this previously equilibrated system was

further subjected to a 20 ps run as an NVE ensemble and the trajectory of several oxygen atoms was traced for 20 ps. Among them, the trajectories of two oxygen atoms represented as atoms A and atom B are shown in **Figure 6**. It is also important to note that at this temperature the atoms are not occupying the ideal lattice site but prefer to remain in the tetrahedral region surrounding the ideal lattice site. The oxygen atom A initially occupying a position (0.75, 0.75, 1.75) migrates to a position (0.75, 1.25, 1.75) with a jump time of ~0.035 ps. The actual atomic positions of the atom A can be obtained by multiplying these atomic positions by the equilibrium lattice parameter as shown in **Figure 6**. Atom A resides in the initial position (0.75, 0.75, 1.75) for 11.13 ps and then migrates to (0.75, 1.25, 1.75) position through a octahedral interstitial position (0.50, 0.50, 1.50). On the other hand, atom B, initially occupying position (5.25, 3.25, 1.75) migrates to position (5.25, 2.75, 1.75) with a jump time of ~0.053 ps. Then it moves to a position (4.75, 2.75, 1.75) with a jump time of ~0.1 ps. Atom B resides in its initial and intermediate positions for 5.80 ps and 9.45 ps, respectively. Analysis of these results indicates that the oxygen atoms jump from one tetrahedral position to another. At any given instant the probability of an atom sitting in the octahedral position is rather small which is in accordance with the MD calculated migration barrier values along [001], [110] and [111] directions. A very low migration barrier along <001> provides oxygen atoms with an easy migration path for random diffusive jumps in the superionic state. Similar result have been reported for UO_2 [12,13], β-PbF_2 [14] and CuI [50,51].

Neutron diffraction studies using single crystal β-PbF_2 showed that the octahedral sites are not significantly occupied at $T > T_c$ [12]. Instead, an appreciable fraction of the anion lattice sites are vacant and located at the F1 and F2 sites. The former was considered to be the location of the 'true' Frenkel interstitials, situated between the midpoint of the two nearest neighbour anion sites and the centre of an anion cube in <110> directions, whilst the latter was attributed to nearest neighbour lattice anions relaxed away from their regular sites in <111> directions towards the centers of adjacent empty anion cubes [12]. This leads to the construction of the two defect cluster models labelled 3:1:2 and 4:2:2 (where the v : i : r notation is number of vacancies : Frenkel interstitials : relaxed anions) [12]. For UO_2 [10,11] a detailed description of a similar model is given in section 1. Similar results have also been reported for γ-CuI [50,51] where the ionic density distribution shows no or very little occupation of the octahedral sites with increasing temperature. The MD calculated average potential energy curves obtained for γ-CuI [50] depict that the energy is a minimum for Cu^+ migration at the tetrahedral sites and rises rapidly at the position of the octahedral site.

H. Temperature variation of single crystal elastic constants

In order to calculate the mechanical stability of ThO_2 as a function of temperature MD calculated elastic constant values as a function of temperature were calculated. **Figure 7** presents our MD calculated single crystal elastic constants (C_{11}, C_{12} and C_{44}) as a function of temperature (300-2900 K range) and room temperature single crystal elastic constant values measured by Macedo et al. [40]. Our MD calculated elastic constant values at 300 K are also listed in **Table 1** for comparison with our GGA and LDA+*U* calculated values (at 0 K) and experimentally reported values at room temperature. The MD calculated C_{12} value matches well with experiment, but C_{11} and C_{44} are underestimated (by < 6%). We have plotted MD calculated elastic constant data upto 2900 K only, as the transition of the oxygen sublattice to the superionic states above this temperature did not allow us to employ this methodology.

In our previous discussion it was found that increasing temperature (represented by isotropic strain) resulted in a significant change in B_{1u} and E_u phonon modes, which in turn changed the elastic properties of single crystal ThO_2. From our MD calculated results it was found that C_{11} shows the most softening, which is one of the pertinent characteristics of the superionic transition. C_{12} and C_{44} also get softened but the rate of decrease of C_{11} is higher compared to other elastic constants, as temperature increases. At this point, it is also important to note that the value of C_{12} becomes less than C_{44} around 2750 K. Our results show that the phase stability criteria: $C_{11}+2C_{12} > 0$, $C_{11}-C_{12} > 0$ and $C_{44} > 0$ are satisfied at all temperatures (dilational lattice strain) including the temperature (dilational lattice strain) corresponding to the superionic regime where the B_{1u} phonon mode is imaginary. Thus, the fluorite phase of ThO_2 remains elastically stable upto the superionic regime. Further, calculations of bulk, shear and Young modulus were performed and MD calculated values were compared to previous experimentally reported values shown in **supplementary information (Figure SI-6)**.

Moreover, oxygen atom displacement pattern corresponding to B_{1u} mode (in ThO_2) beyond harmonic region essentially leads to a phase change to a tetragonal structure in ZrO_2 and HfO_2. However, experimental data on phase diagram of ThO_2 shows that the cubic structure is the only stable phase upto melting temperature. ThO_2 satisfies mechanical stability criterion ($C_{11}+2C_{12} > 0$, $C_{11}-C_{12} > 0$ and $C_{44} > 0$) for lattice parameters corresponding to superionic state. Therefore, imaginary phonon mode with $\varepsilon = 0.045$ (for GGA, as shown in Figure 2) is indicative of oxygen sublattice melting or Frankel like disordering of oxygen sublattice and not the phase transformation.

4. Conclusions

Combined first-principles and classical molecular dynamics simulations were used to investigate ground state phase stability, lattice dynamical stability and anion transport behaviour as a function of dilational lattice strain (or equivalently temperature). Our GGA, LDA+*U* and MD calculated ground state properties of ThO_2 agree well with experimental and previous theoretical calculations. Calculated phonon dispersion curves along symmetry directions using first principles are in good agreement with reported experimental data at room temperature. With increasing dilational lattice strain (ε), GGA and LDA+*U* calculated B_{1u} and E_u phonon mode frequencies soften at the X point (0, 0, 1). These phonon mode frequencies decrease nonlinearly and B_{1u} mode frequencies become smaller compared to E_u mode frequencies in the range $0.05 > \varepsilon > 0.04$, This is associated with sharp increase in the narrow peak of the phonon density of states when the B_{1u} and E_u modes crosses each other (or are about to cross) at the X point. These implies to higher occupation probability and hence higher coupling probability of these modes at high temperatures. As a result, the anion movement mechanism along <001> directions increase the occupation of interstitial sites. Moreover, NEB MD results of the diffusion barrier show <001> are the easy direction for anion migration. The tracking of anion positions as a function of time in the superionic state in our MD simulations are consistent with a jump diffusion model in which the oxygen ions hop from one tetrahedral site to another via octahedral interstitial sites. These results establish the possible mechanism of anion transport in the neighborhood of the superionic regime, which compared well with similar anionic transport behaviour observed in γ-CuI and β-PbF_2. Finally the calculations are consistent with the fluorite phase of ThO_2 remaining elastically stable upto the superionic regime.

Acknowledgment

We thank the EPSRC for funding as part of the INDO-UK project (grant code EP/K00817X/1). Computational facilities and support were provided by High Performance Computing Centres at Bhabha Atomic Research Centre and Imperial College London.

References

[1] D.A. Keen, J. Phys.: Condens. Matter 14 (2002) R819-857, S. Hull, Rep. Prog. Phys. 67 (2004) 1233–1314.

[2] H.Y. Xiao, Y. Zhang and W.J. Weber, Phys. Rev. B 86 (2012) 054109.
[3] O.J. Staun, L. Gerward, V. Kanchana and G. Vaitheeswaran, J. Alloy. Compd. 381 (2004) 37.
[4] R.C. Linares, J. Phys. Chem. Solids 28 (1967) 1285.
[5] P.S. Ghosh, P.S. Somayajulu, A. Arya, G.K. Dey, B.K. Dutta, Journal of Alloys and Compounds 638 (2015) 172–181.
[6] P.S. Ghosh, P.S. Somayajulu, R. Krishnan, N. Pathak, A. Arya, G.K. Dey, J. Alloys Compd. 650 (2015) 165-177.
[7] P.S. Somayajulu, P.S. Ghosh, A. Arya, K.V. Vrinda Devi, D.B. Sathe, J. Banerjee, K.B. Khan, G.K. Dey, B.K. Dutta, Journal of Alloys and Compounds 664 (2016) 291-303.
[8] P.S. Somayajulu, P.S. Ghosh, J. Banerjee, K.L.N.C. Babu, K.M. Danny, B.P. Mandal, T. Mahata, P. Sengupta, S.K. Sali, A. Arya, Journal of Nuclear Materials 467 (2015) 644-659.
[9] B.T.M. Willis, Proceedings of the Royal Society of London. Series A, Mathematical and Physical Sciences 274 (1963) 134 (part II).
[10] K. Clausen, W. Hayes, J. E. Macdonald and R. Osborn, PHYSICAL REVIEW LETTERS 52 (1984) 1238.
[11] M.T. Hutchings, J. Chem. Soc., Faraday Trans. II, 83 (1987) 1083-1103.
[12] M. H. Dickens, W. Hayes, M. T. Hutchings and C. Smith, J. Phys. C: Solid State Phys. (1982), 15, 4043.
[13] D.F. Fischer, Journal of Nuclear Materials 102 (1981) 220-222.
[14] H. Nafe, Solid State Ionics 13 (1984) 255-263.
[15] D.K. Hohnke, Solid State Ionics 5 (1981) 531-534.
[16] M. T. Hutchings et al., J. Phys. C: Solid State 17, 3903 (1984).
[17] B. Voronin and S. Volkov, J. Phys. Chem. Solids 62, 1349 (2001).
[18] C. R. A. Catlow, Comments Solid State Phys. 9, 157 (1980).
[19] A. Chadwick, Solid State Ionics 8, 209 (1983).
[20] A. R. Allnatt, A. V. Chadwick, and P. W. M. Jacobs, Proc. R. Soc. A 410, 385 (1987).
[21] B. Voronin, J. Phys. Chem. Solids 56, 839 (1995).
[22] C. R. C. Catlow, Proc. R. Soc. Lond. A 353 (1977) 533.
[23] K. Bakker, E.H.P. Cordfunke, R.J.M. Konings, R.P.C. Schram, J. Nucl. Mater. 250 (1997) 1–12.
[24] G. Kresse and J. Furthmueller, Phys. Rev. B: Condens. Matter Mater. Phys. 5 (1996) 11169.
[25] G. Kresse and J. Furthmueller, Comput. Mater. Sci. 6 (1996) 15.

[26] P. E. Blo¨chl, Phys. Rev. B: Condens. Matter Mater. Phys. 50 (1994) 17953.
[27] J. P. Perdew, K. Burke and M. Ernzerhof, Phys. Rev. Lett. 77 (1996) 3685.
[28] S.L. Dudarev, G.A. Botton, S.Y. Savrasov, C.J. Humphreys, A.P. Sutton, Phys. Rev. B 57 (1998) 1505.
[29] H. J. Monkhorst and J. D. Pack, Phys. Rev. B: Condens. Matter Mater. Phys. 13 (1979) 5188.
[30] A. Togo, F. Oba and I. Tanaka, Phys. Rev. B 78 (2008) 134106.
[31] R. M. Pick, M. H. Cohen, and R. M. Martin, Phys. Rev. B 1, 910 (1970).
[32] P. Giannozzi, S. de Gironcoli, P. Pavone, and S. Baroni, Phys. Rev. B 43, 7231 (1991).
[33] X. Gonze and C. Lee, Phys. Rev. B 55, 10355 (1997).
[34] S. Plimpton, J. Comput. Phys. 117 (1995) 1-19.
[35] P.P. Ewald, Ann. Phys. 64 (1921) 253.
[36] M.W.D. Cooper, M.J.D. Rushton, R.W. Grimes, J. Phys. Condens. Matter 26 (2014) 105401 (10 pp).
[37] R. Hill, Proc. Phys. Soc. London 65 (1952) 349; W. Voigt, Ann. Phys. (Leipzig) 38 (1889) 573; A. Reuss, Z. Angew. Math. Phys. 9 (1929) 49.
[38] J. Staun Olsen, L. Gerward, V. Kanchana, G. Vaitheeswaran, Journal of Alloys and Compounds 381 (2004) 37–40.
[39] M. Idiri, T. Le Bihan, S. Heathman, J. Rebizant, Phys. Rev. B 70 (2004) 014113.
[40] P.M. Macedo, W. Capps and J.B. Watchman, J. Am. Ceram. Soc. 47 (1964) 651.
[41] K. Clausen, W. Hayes, E. J. Macdonald, R. Osborn, and G. P. Schnabel, J. Chem. Soc., Faraday Trans. II, 83 (1987) 1109.
[42] J.D. Axe and G.D. Pettit, Phys. Rev. 151 (1966) 676-680.
[43] Y. Lu, Y. Yang and P. Zhang, J. Phys.: Condens. Matter 24 (2012) 225801 (10pp).
[44] C. Sevik and T. Çağın, Phys. Rev. B 80 (2009) 014108 (7pp).
[45] A. Jayaraman, G.A. Kourouklis and L.G. Van Uitert, Pramana J. Phys. 30 (1988) 225-231.
[46] J.L. Gavartin, C.R.A. Catlow, A.L. Shluger, P.W.M. Jacobs, Z.A. Rycerz, Radiat. Defects Solids 134, 107 (1995).
[47] A. Nakano, Comp. Phys. Commun. 176 (2008) 280.
[48] G. Henkelman, H.A. Jonsson, J. Chem. Phys. 113 (2000) 9978.
[49] G. Henkelman, B.P. Uberuaga, H. Jonsson, J. Chem. Phys. 113 (2000) 9901.
[50] J. X. M. Zheng-Johannson and R. L. McGreevy, Solid State Ionics 83, 35 (1996).

[51] K. Ihata and H. Okazaki, J. Phys.: Condens. Matter 9, 1477 (1997).

Tables

Table 1: Calculated structural, elastic and dielectric properties of ThO_2 are compared with previous experimental and theoretical results in the literature.

Properties	This work			Previous Experimental Work	Previous Theoretical Work	
	GGA	LDA+*U*	MD		GGA	LDA+*U*
a_0 (Å)	5.618	5.595	5.596	5.598(4) [38], 5.6001(3) [39], 5.597 [6]	5.619 [43]	5.60 [44]
B_0 (GPa)	187.4	209.3	192.9	195.3±2.0 [38], 198(2) [39]	190 [43]	216 [44]
B_0'	4.23	4.28		5.4±0.2 [38], 4.6(3) [39]	4.3 [43]	
C_{11} (GPa)	352.2	375.4	351.9	367 [40], 377 [41]	351.2 [43]	381 [44]
C_{12} (GPa)	107.8	129.8	113.6	106 [40], 146 [41]	106.9 [43]	134 [44]
C_{44} (GPa)	74.6	105.8	71.7	79 [40], 89 [41]	74.1 [43]	106 [44]
ε^{∞}	4.83	4.74		4.86 [42]	4.83 [43]	
Z* Th	5.41	5.38		-	5.41 [43]	5.327 [44]
Z* O	-2.71	-2.69		-	-2.71 [43]	-2.663 [44]

Table 2: GGA and LDA+*U* calculated phonon mode frequencies of ThO_2 at high symmetry points of the Brillouin zone (Γ, X and L) are compared with inelastic neutron scattering and Raman scattering measured phonon frequencies. The results are shown for isotropic lattice strain (ε) of 0.00.

Symmetry point	Strain ε = 0.00		
	Mode	GGA	LDA+*U*	Expt.
Γ	F_{1u} (LO)	16.6	17.3	16.9 [41], 17.0 [45]
	F_{2g}	13.1	14.2	14.1 [41], 13.9 [45]
	F_{1u} (TO)	7.9	9.0	8.3 [41], 8.4 [45]
X	A_{1u}	17.9	18.4	
	E_u	12.7	13.4	13.3 [41]
	A_{2u}	6.7	8.6	
	E_g	6.7	7.0	5.7 [41]
	B_{1u}	5.6	6.9	
	E_u	3.1	3.5	3.6 [41]
L	A_{1u}	16.2	16.9	
	A_{1g}	11.8	12.7	12.2 [41]
	E_u	11.5	12.4	11.2 [41]
	E_g	9.7	10.6	10.7 [41]
	A_{1u}	5.2	5.8	5.3 [41]
	E_u	2.6	2.8	2.9 [41]

Figures

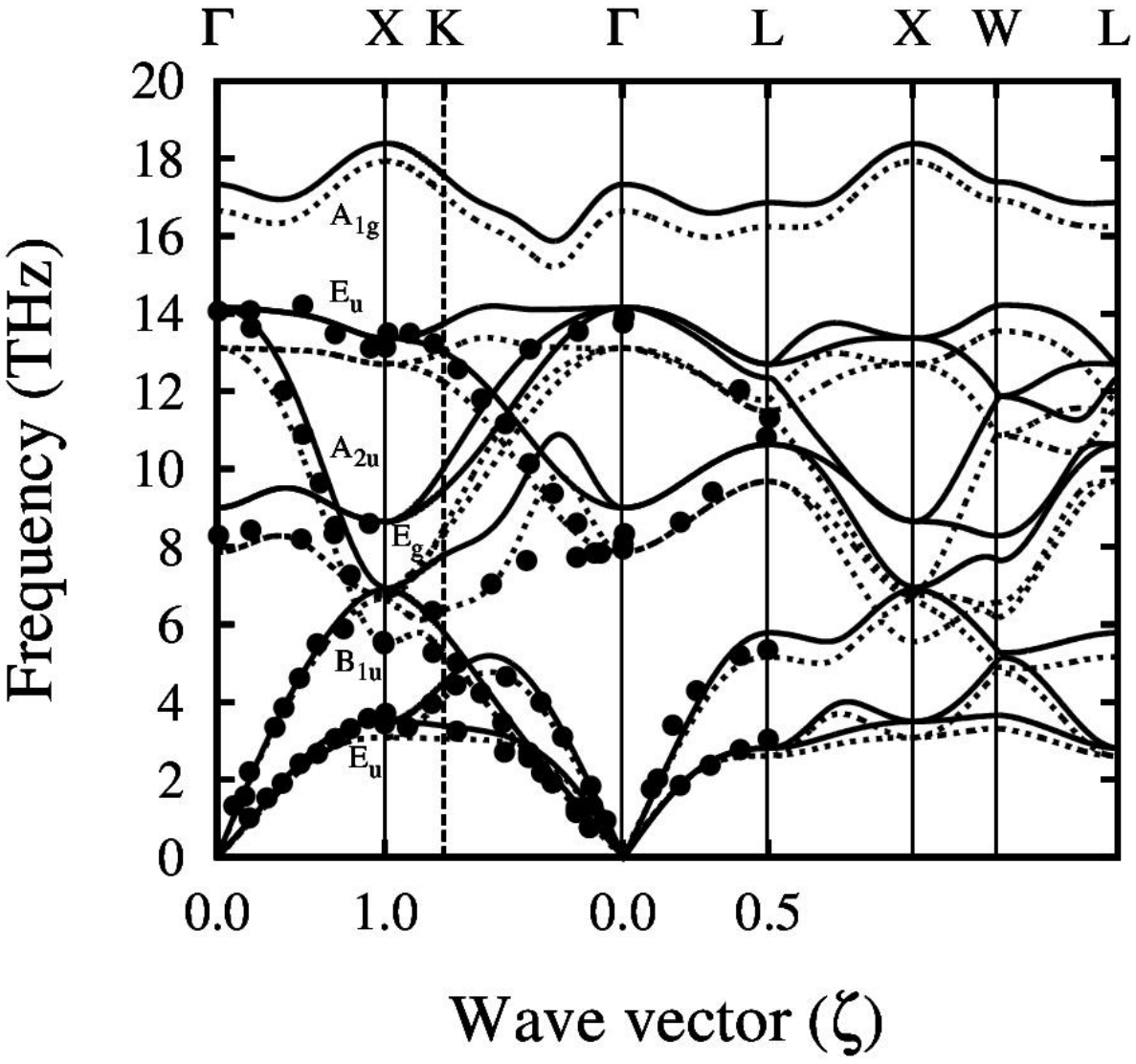

Figure 1: Phonon dispersion curve of ThO_2 calculated using GGA and LDA+*U* compared with inelastic neutron scattering data [41] and Raman scattering measured data [45] at room temperature. Solid and dotted line represents LDA+*U* and GGA calculated phonon frequencies, respectively. Solid circles present experimentally measured data. The notation of the special points is *Γ* (0, 0, 0), *X* (0, 0, 1), *W* (1, 1, 0) and *L* (1, 1, 1) .

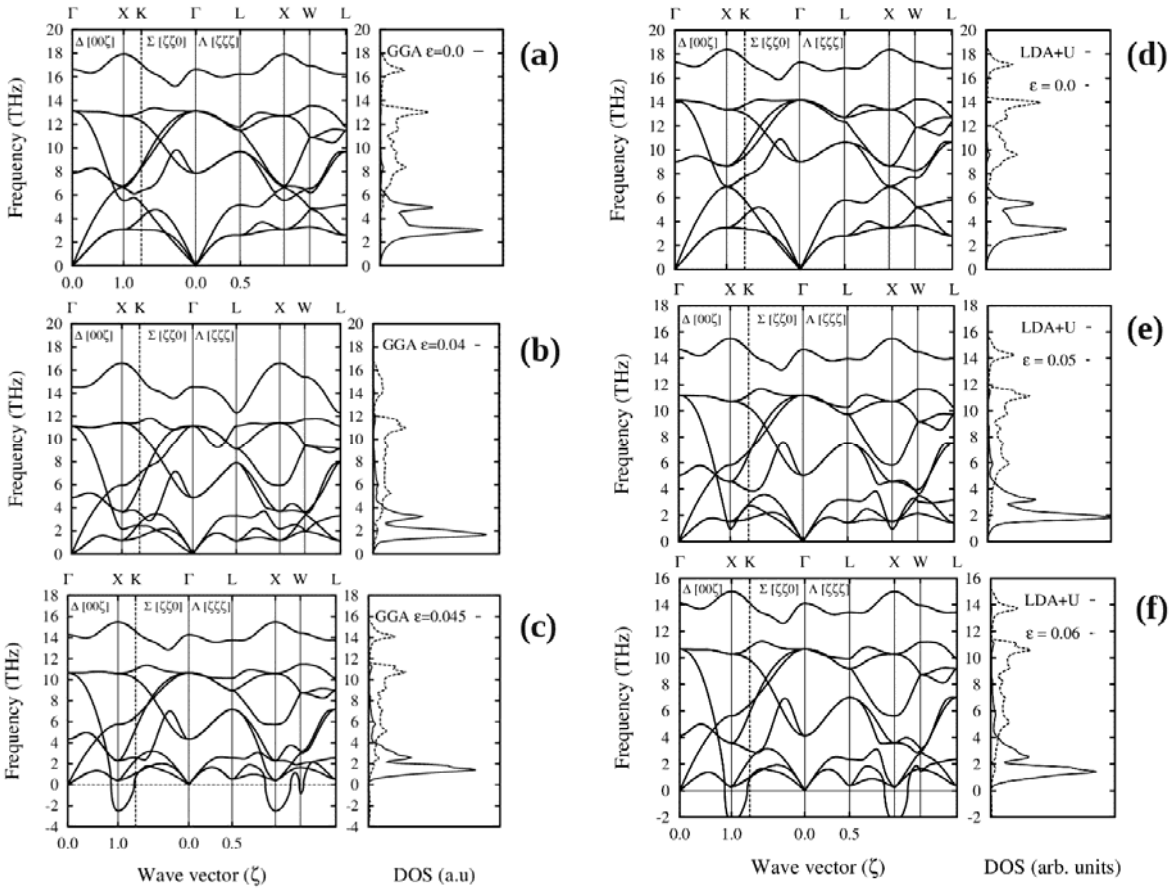

Figure 2: Phonon dispersion curve and density of states for ThO_2 calculated using GGA at lattice strain (a) ε = 0.0, (b) ε = 0.04, (c) ε = 0.045 and using LDA+*U* at lattice strain (d) ε = 0.0, (e) ε = 0.05, (f) ε = 0.06.

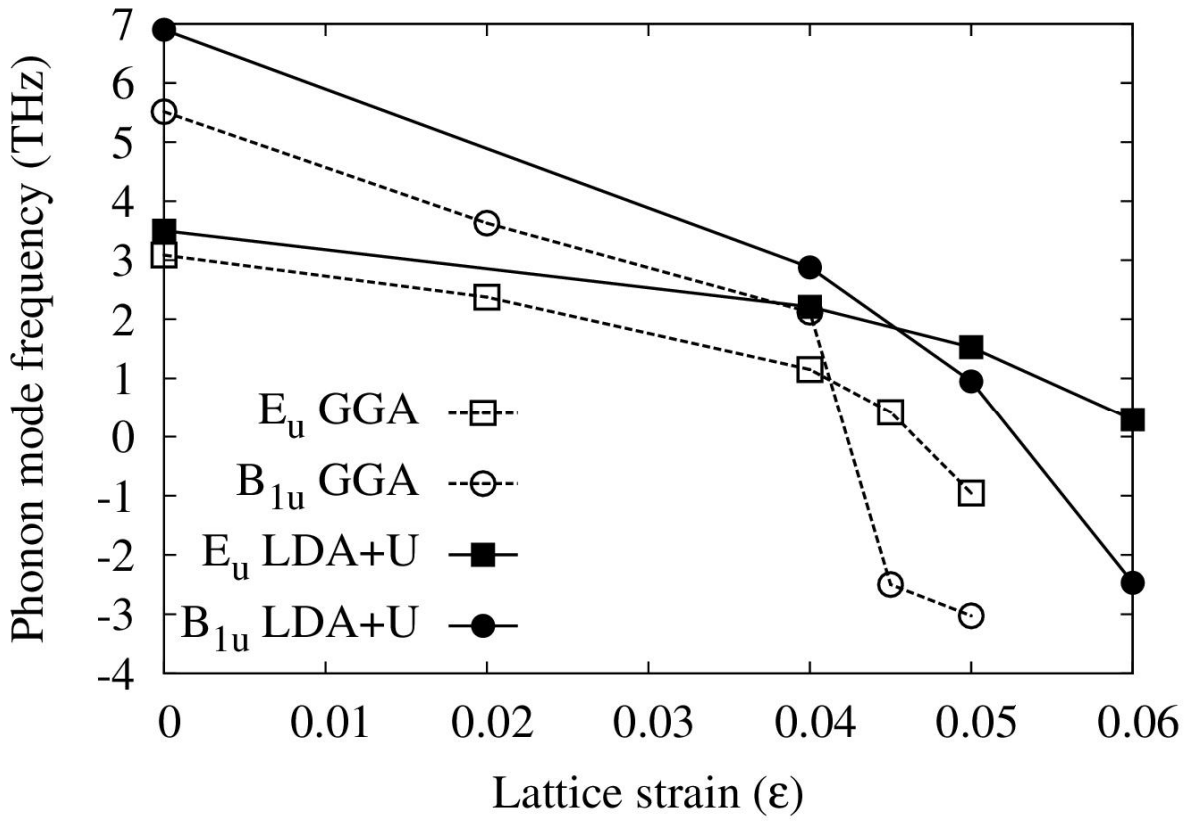

Figure 3: GGA (solid points) and LDA+*U* (empty points) calculated B_{1u} and E_u mode frequencies at the X point as a function of linear lattice strain.

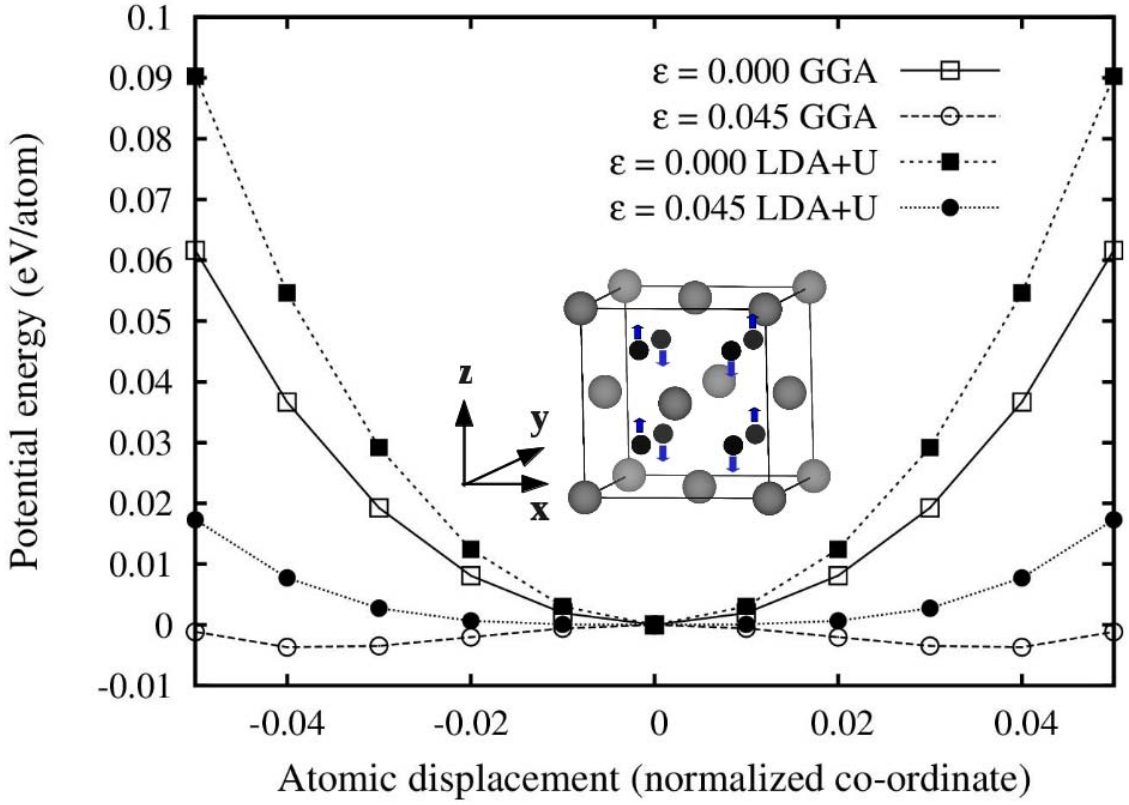

Figure 4: GGA and LDA+*U* calculated variation of potential energy versus zone center phonon mode B_{1u} in terms of normalized atomic displacement of O atoms as a function of isotropic dilational lattice strains. Actual motion of the O atoms in the ThO_2 unit cell is also shown.

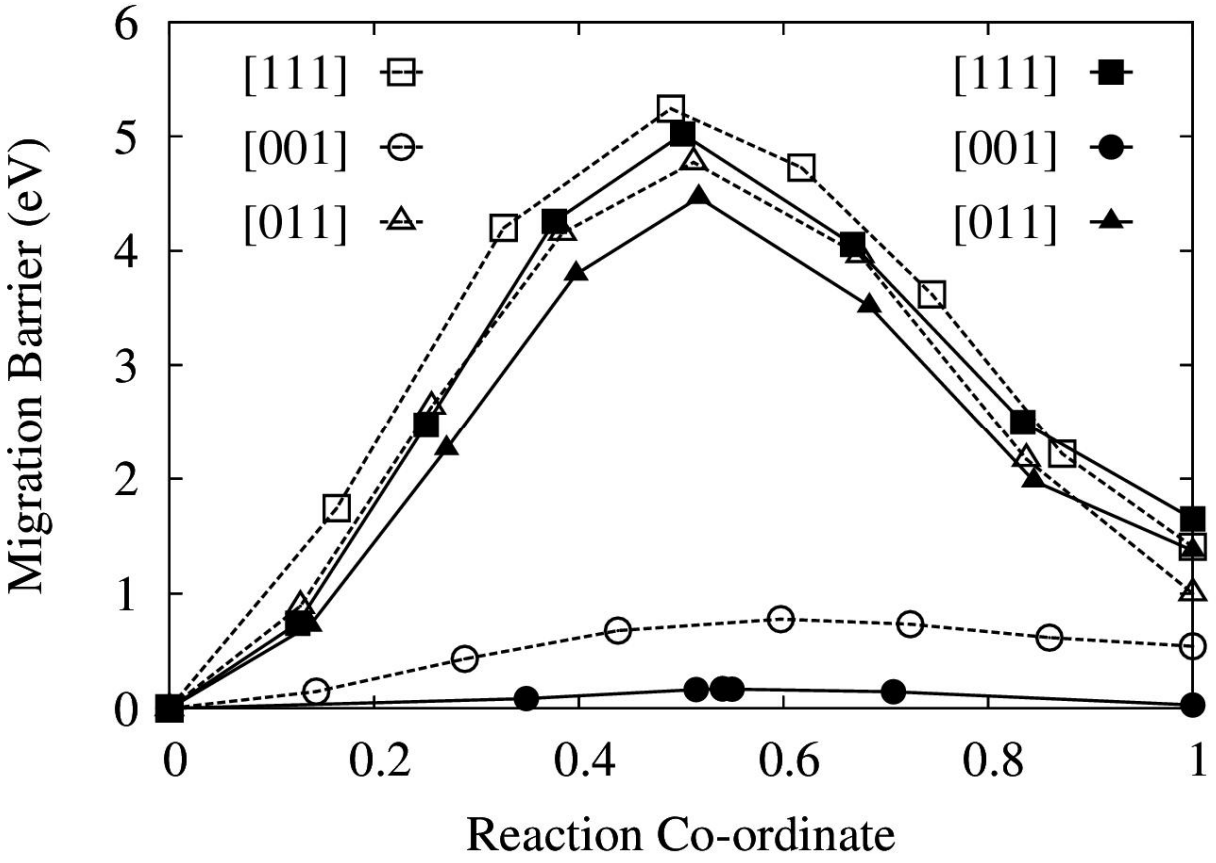

Figure 5: MD calculated migration barrier along [001], [110] and [111] high symmetry directions. Solid lines and fill points present MD NEB calculated migration path for a = 5.6 Å (correspond to normal state). Similarly, doted lines and open points present MD NEB calculated migration path for a = 5.8 Å (corresponds to superionic state).

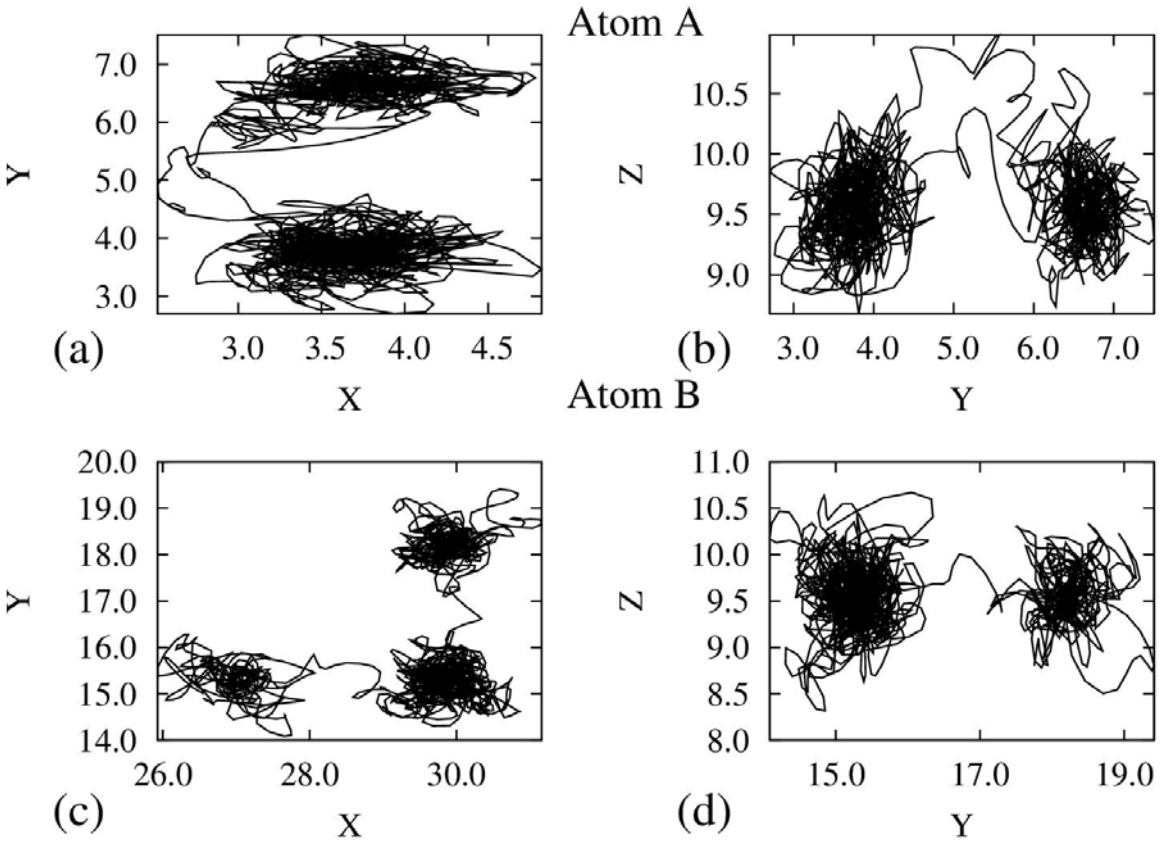

Figure 6: Snapshot of the movement of given oxygen atoms (atom A and atom B) for 20 ps time duration in the XY and YZ plane calculated using molecular dynamic simulations at 3000 K. Oxygen atoms preferentially occupy and migrate through tetrahedral positions.

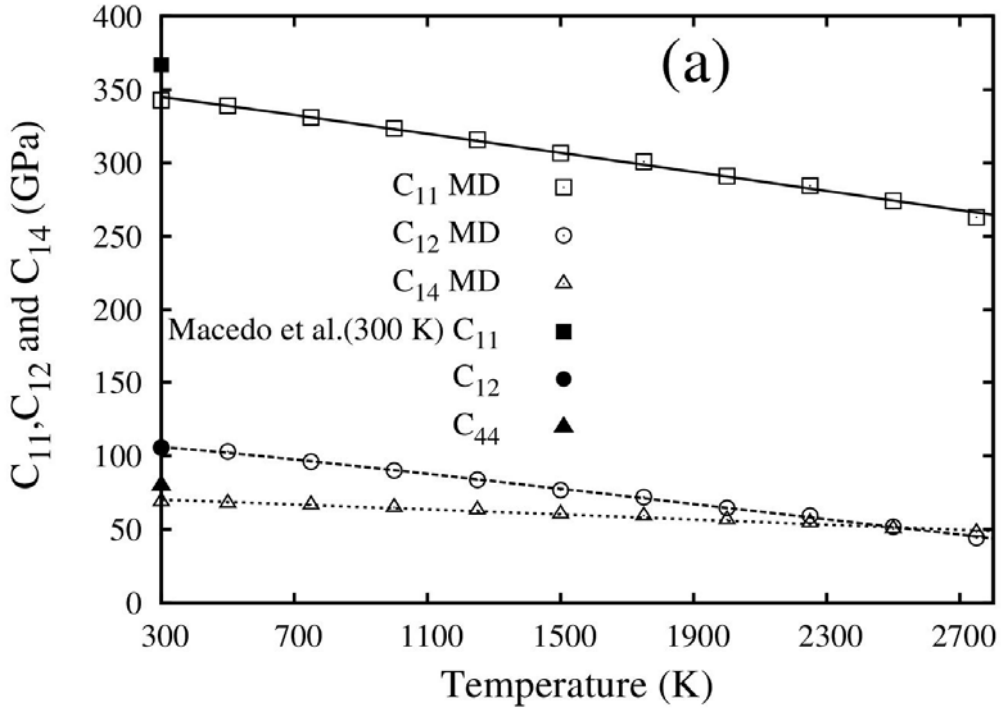

Figure 7: MD calculated single crystal elastic constants (C_{11}, C_{12} and C_{44}) are shown as a function of temperatures (300-2900 K range) and experimentally measured room temperature values are also shown (measured by Macedo et al. [40] from single crystal ThO_2).